Journal of Materials Chemistry A

Accepted Manuscript

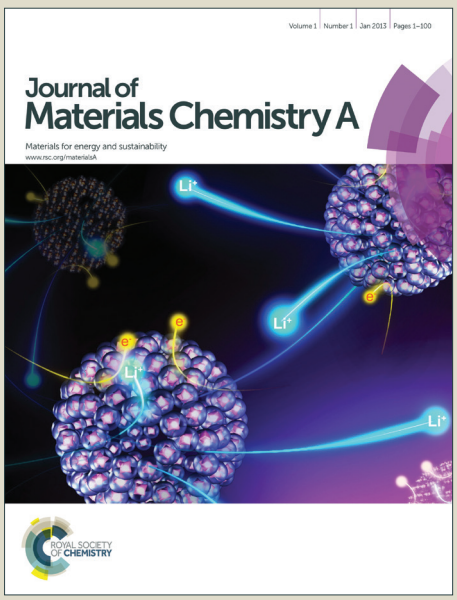

ROYAL SOCIETY OF CHEMISTRY

www.rsc.org/materialsA

Core-shell ZnO/$ZnFe_2O_4$@C Mesoporous Nanospheres with Enhanced Lithium Storage Properties towards High-performance Li-ion Batteries

*Changzhou Yuan *, Hui Cao, Siqi Zhu, Hui Hua, Linrui Hou**

[*] *Prof.* C. Z. Yuan, H. Cao, S. Q. Zhu, *H. Hua, Prof.* L. R. Hou
School of Materials Science & Engineering, Anhui University of Technology, Ma'anshan, 243002, PR China Email: ayuancz@163.com; houl629@163.com

Prof. C. Z. Yuan

Chinese Academy of Science (CAS) Key Laboratory of Materials for Energy Conversion, Hefei, 230026, P.R. China

Key words: ZnO/$ZnFe_2O_4$@C nanospheres; Core-shell; Mesoporous; Anode; Li-ion Batteries

Abstract

In this contribution, we rationally developed and explored an appealing multi-featured nanoarchitecture, core-shell mesoporous ZnO/$ZnFe_2O_4$@C (ZZFO@C) nanospheres, for highly reversible lithium storage. Physicochemical characterizations revealed that the mixed ZZFO nanospheres with rich mesopores, and even yolk-shell hollow structure were coated uniformly with a ultrathin N-doped carbon shell of ~10 nm in thickness, and endowed with the internal continuous carbon network meanwhile. Benefitting from striking synergy and interplay of intrinsic component effect and structural advantages, the as-fabricated core-shell ZZFO@C exhibited superior electrochemical Li-storage performance with high specific capacity, excellent cycling property and good rate capability when evaluated as an anode material for rechargeable Li-ion batteries (LIBs). These findings further revealed that the resulting core-shell ZZFO@C would be a promising anode for high-performance LIBs. Furthermore, the in-depth insights into the structure/component–Li-storage correlation of the core-shell ZZFO@C hybrid significantly favored for optimizational design, and efficient fabrication of advanced hybrid anodes for next-generation LIBs in the future.

1. Introduction

In last decades, the Li-ion battery (LIB) market is growing rapidly beyond expectations, which greatly stimulates the tremendous research interests to exploring low-cost yet high-performance electrodes for advanced LIBs of large specific capacity and/or power to meet the ever-growing demands for large-scale powering systems of electric and/or hybrid vehicles, and smart gird storage, apart from the nowadays-established consumer electronics.[1-3] Up till now, graphite has been established as a common anode material for the state-of-the-art LIBs, characterized by its low cost, long cycling life and environmental friendliness.[2-4] Unfortunately, graphite-based anodes intrinsically possess relatively low theoretical capacity of ~372 mAh g^{-1}, and particularly near zero potential for lithium intercalation reaction, rendering potential safety concerns, such as, dendrite formation and short-circuiting of LIBs. It is therefore crucial and significant to explore even safer anodes with larger theoretical capacity and higher Li-intercalation potential compared to the graphite anode.

Since the pioneer work of transition-metal oxides (TMOs) as anodes for LIBs in 2000 by Poizot *et al.*,[5] interstitial-free 3d TMOs (Me_xO_y, Me = Co, Ni, Cu, Fe, *etc.*) have been reported extensively for LIBs, owing to its high theoretical capacity (500 – 1000 mAh g^{-1}), far higher than those of graphite-based anodes. In recent years, ternary spinel mixed TMOs, smartly combinating two simple TMOs, or a TMO and post-TMO, are emerging as promising anodic materials for next-generation LIBs, thanks to their higher electrochemical activities and better electronic conductivity determined by the complex chemical compositions and synergetic effects *via* a suitable combination of different TMOs.[2, 6] Many reports on the fabrication and electrochemical Li-storage properties of ternary mixed TMOs can be retrieved well, including $MeMn_2O_4$ (Me = Fe, Mg, Zn, Cu, *etc.*),[7-9] $MeCo_2O_4$ (Me = Zn, Co, Ni, *etc.*),[9-11] $MeFe_2O_4$ (Me = Co, Ni, Cu, Zn, *etc.*),[2, 3, 12-16] and so on. Remarkably, iron is more environmentally benign, much cheaper and more abundant in nature compared to the cobalt and manganses species. In particulalry, among the ferrite family, $ZnFe_2O_4$

(denoted as ZFO hereafter),[13-15, 17-21] where divalent (Zn^{2+}) ions and trivalent (Fe^{3+}) ions occupy tetrahedral (A) and octahedral (B) sites being represented as $(Zn_{1-x}^{2+}Fe_x^{3+})[Zn_x^{2+}Fe_{2-x}^{3+}]O_4$, stands out from others as one more competitive anode, benefiting from the low price, abundance, and environmental friendliness of both Zn and Fe species, even lower working voltage of ~1.5 V for lithium extraction, and most importantly, high theoretical specific capacity (~1072 mAh g^{-1}) originating from both the conversion and alloying reaction of "LiZn-Fe-Li_2O composite" for reversible lithium storage.[13-15, 17-21]

Nevertheless, its practical application is still impeded seriously by fast capacity fading and poor rate capability resulting from inherent low electronic conductivity, severe agglomeration and large volume change during the lithiation/delithiation process. To solve these problems, one strategy is to synthesize carbon-based hybrids,[9, 17, 22] *i.e.*, embedding the electroactive ZFO in cushioning carbonaceous medium. For such case, the conductive confining matrix can effectively enhance the electronic conductivity, and buffer the volume changes of the ZFO upon cycling while preventing them from aggregation, which synchronously prolongs the cycling life and improves the rate behaviors of the ZFO anodes. Particularly, it has been verified from first principle calculaions that N-doped carbon-coating can enhance the interfacial stability and electronic conductivity, rendering improved electrochemical kinetics.[23, 24] Besides this, an emerging concept is the smart hybridization of bi-component TMOs, such as, ZnO/ZFO,[3, 13, 25] $Fe_2O_3/NiFe_2O_4$,[26] $CoO/CoFe_2O_4$,[27] Fe_2O_3/ZFO,[28] MnO_2/Fe_2O_3[29] and Fe_2O_3/Co_3O_4,[30] in which high capacity, remarkable rate capability and cycling life are commonly expected *via* the synergistic effec of each component, compared with their single-component counterparts. However, it is still a challgeable topic to construct an intergrated architecture *via* a facile strategy, where structural features and electroactivities of each component are fully manifested, and the interface/chemical distribution are homogeneous at the nanoscale.[27] In addition, it is also of great significance to pass the electrodes from bulk to delicated hollow/mesoporous nanostructures with a large specific surface area (SSA), short diffusion path and enhanced reactivity, wherein not only is the Li^+ diffusion much easier, but also the strain

asscociated with Li^+ intercalation is better accommodated, resulting in significantly enhanced electrochemical performance.[31, 32] Despite the advantages of the aforementioned strategies, of particular note, each design applied alone generally results in limited improvement in the whole electrochemical Li-storage properties of any electrode. In this regards, the fabrication of truly durable ZFO-based anodes with satisfactory cycling ability and large capacity meanwhile is till highly desirable for next-generation advanced LIBs *via* an intergrated solution.

Inspired by previous efforts and huge contributions, in this study, we have rationally explored a multi-featured nanoarchitecture of N-doped carbon coating ZnO/ZFO (designed as ZZFO afterwards) mesoporous nanospheres, *i.e.*, core-shell ZZFO@C nanospheres, for highly reversible lithium storage. This unique intergrated methodology incorporated several desirable design rationales for high-performance anode materials based on mesoporous and/or yolk-shell hollow nanostructures, N-doped carbon nanocoating and ZnO/ZFO heterojunctions at the nanoscale. In favor of the synergy and interplay of the component effect and intirisic structural advantages, the core-shell ZZFO@C mesoporous nanospheres exhibited an exceptional cycling performance over 500 cycles and enhanced high-rate capacibility when evaluated as an intriguing anode for high-performance LIBs.

2. Experimental Section

2.1 Synthesis of core-shell ZZFO@C product

All the chemicals were analytic-grade, and used directly without further purification. The synthesis of the mesoporous ZZFO nanospheres were prepared as follows. A mixture solution (80 mL) of absolute ethanol and de-ionized (DI) water (V : V, 1 : 7) was obtained. 0.329 g of $K_3Fe(CN)_6$ was dissolved into 60 mL of the above mixture solution to form a transparent solution firstly (solution A). Then, 0.329 g of $Zn(CH_3COO)_2{\cdot}2H_2O$ is dissolved into another 20 mL of the mixture solution to form a transparent solution (solution B). The two solutions were both transferred to an ice bath. After stirred for 10 min, the solution B was taken out from the ice bath,

and then added into the solution A drop by drop under vigorously stirred in ice bath. After further stirred in ice bath for another 2 h, the mixed solution was transferred into a refrigerator, keeping at 4 ºC in a refrigerator for 24 h. Then, the precipitate was filtered, and washed several times with DI water and absolute ethanol for several times, respectively. After dried for 24 h, the deep yellow product was obtained, annealed in air at a temperature of 500 ^{o}C for 2 h in an electric oven with a temperate ramp of 1 ºC min^{-1}. The ZZFO sample was fabricated accordingly.

Then, 0.16 g ZZFO was dispersed in 30 mL Tris-buffer with a pH of ~8.5 under ultrasonication. Next, 30 mg dopamine was added to the suspension under stirring, and the mixture was subjected to continuously stirring for 24 h at ~25 °C. Afterwards, the precipitate was collected and dried in air. The specimen was annealed in a quartz tube to 150 °C and maintained at the temperature for 1 h in N_2 atmosphere, then further heated to 500 °C with a ramping rate of 5 °C min^{-1}, and kept at this temperature for 5 h. The ZZFO@C was obtained accordingly.

2.2 Materials characterization

The samples were examined by powder X-ray diffraction (XRD) (Max 18 XCE, Japan) using a Cu K*a* source (λ = 0.154056 nm) at a scanning speed of 3° min^{-1} over a 2θ range of 10 – 80 °. The pattern was analyzed by the Rietveld refinement methode by using the software RIETAN-FP. Schematic illustrations of the crystal structures were drawn by using the program VESTA. The morphologies and structures were observed with field-emission scanning electron microscopy (FESEM, JEOL-6300F, 15 kV), transmission electron microscope (TEM), high-resolution TEM (HRTEM), energy dispersive X-ray analysis (EDXA) and selected area electron diffraction (SAED) (JEOL JEM 2100 system operating at 200 kV). Thermogravimetric (TG) analysis was carried out under air flow with a temperature ramp of 10 °C min^{-1} from room temperature to 800 °C. N_2 adsorption/desorption was determined by Brunauer-Emmett-Teller (BET) measurement by using an ASAP-2010 surface area analyzer. Raman analysis of the sample was recorded by Laser Raman (T6400, Jobion yzon corp. France)

2.3 Electrochemical measurements

The working electrode consisted of the as-obtained ZZFO@C or ZZFO, conductive material (acetylene black, Super-P-Li) and environmentally friendly, water-based Na-carboxymethyl cellulose (CMC, average M_w: ~250 000) in a weight ratio of 70 : 20 : 10 with DI water as a solvent upon the copper foil substrate, and dried at 100 ºC for 12 h to remove the solvent in a vacuum oven. The electrolyte used here was 1 M $LiPF_6$ in a mixed solvent of ethylene carbonate (EC), dimethylcarbonate (DMC) and diethyl carbonate (DEC) (1 : 1 : 1, v/ v/ v) as the electrolyte. Celgard 2400 membrane was used as the separator. The cell assembly was carried out in an Ar-filled glovebox with both the moisture and oxygen content below 0.5 ppm. Prior to characterization, the cells were all aged for 24 h. Galvanostatic charge/discharge tests were performed by using a Land-CT2001A (Xinnuo, Wuhan, China) with a voltage window of 0.01 – 3.00 V (*vs.* Li^+/Li) at various setting current rates. The cyclic voltammetry (CV) in the potential window of 0.01 to 3.00 V (*vs.* Li/Li^+) and electrochemical impedance spectroscopy (EIS) over the frequency range of 100 kHz to 0.01 Hz were carried out by using an IVIUM electrochemical workstation (Ivium Technologies, the Netherlands) at ~25 ºC.

3. Results and discussion

3.1 Physicochemical, textural and structural characterizations

Herein, we first devise a simple bottom-up synthetic protocol to successfully fabricate unique core-shell ZZFO@C mesoporous nanospheres, as schematically illustrated in **Fig. 1a**. Initially, a typical solid–solution precursor (marked as ZFC henceforward) of deep yellow Prussian blue analogue consisting of $Zn_3[Fe(CN)_6]_2$ (JCPDS No. 38-0688) and $Zn_3[Fe(CN)_6]_2 \cdot xH_2O$ (JCPDS No. 38-0687), is controllablly prepared *via* the simple reaction of $K_3Fe(CN)_6$ and $Zn(CH_3COO)_2 \cdot 2H_2O$, and no any detectable impurity phases are detected, as examined by powder XRD measurement (**Fig. S1**, Electronic Supporting Information, ESI†). With following calcination of ZFC at 500 ºC in air, a significant weight loss, commongly attributed to the escape of organic molecules, and absorbed/crystal water in the ZFC, is estimated as ~42 wt.% totally before complete decomposition,

as inspected in TG analysis (**Fig. S2**, ESI†). Accordingly, the as-obtained ZFC is *in-situ* coverted into the mixed phase of ZFO and ZnO with homogenerous dispersion at the nanoscale *via* thermally induced oxidative decomposition. As seen from typical wide-angle XRD pattern for the resulting mahogany ZZFO (**Fig. S3**, ESI†), the characteristic diffraction reflections clearly reveal the two-phase co-existence of the cubic ZFO (JCPDS file no. 65-3111) and hexagonal ZnO (JCPDS file no. 36-1451) phases derived from the ZFC. Then, a conformal polymer layer is continuously coated upon the surface of the resulting ZZFO, which benefits from the catecholic group of polydopamine (PDA) coordinating with Fe^{3+} of ZFO.[17] A core-shell structure of ZZFO@polydopamine (ZZFO@PDA) is obtained through an oxidation an cyclization reaction of dopamine.[33, 34] As a result, a unique core-shell ZZFO@C nanoarchitecture with N-doped carbon shell (~12.3 wt.% loading, **Fig. S4**, ESI†), owing to the high-percent N species in the PDA, is finally obtained by thermally annealing in N_2 at 500 °C.

The crystallographic structure of the as-synthesized black ZZFO@C, as evident in optical image (see the inset in panel b), was analyzed by powder XRD pattern (**Fig. 1b**). And corresponding Rietveld refinement was finely conducted according to the refined parameters (**Table S1**, **S2**, ESI†). Indexing the pattern explicitly presents that a blend of a ZFO Fd-3m(227) cubic structure and a ZnO P63mc(186) hexagonal structure (see the insets in panel b) is prepared, as seen in **Fig. 1b**, which is in good agreement with that of the core ZZFO (**Fig. S3**, ESI†). Furthermore, all refinements give a small value of factors including R_{wp} (6.34%), R_p (5.04%) and S (1.84), indicative of a good and reliable structural analysis. According to the refinement data, the ratio of the ZnO/ZFO is approximately estimated as 2.5 : 1. As discussed above, it is easy to conclude that there is no any obvious influence of carbon-coating process upon the composition of the core. Remarkably, it is worthy of noting that no any identifiable peaks corresponding to the carbonaceous shell is observed, suggesting its amorphous nature, which is further evidenced by corresponding Raman data (**Fig. S5**, ESI†).

More detailed chemical and bonding environments of the resultant core-shell ZZFO@C sample were further ascertained by XPS measurements. The overview survey spectrum (**Fig. S6**, ESI†) of the resulting ZFO@C sample reveals the concomitance of Fe, Zn, O, C and N species in the final specimen. As depicted in **Fig. 2a**, the high-resolution Fe 2p spectra are finely fitted for the ZZFO@C and ZZFO samples, and both investigated considering two spin-orbit doublets, where no discernable differences are observed. Specifically, the fitting peaks locating at binding energies (BEs) of ~711.3, ~713.2, ~718.6 and ~725.5 eV are corresponding well to the tetrahedral Fe $2p_{3/2}$, octahedral Fe $2p_{3/2}$, the shake-up satellite structure and the Fe $2p_{1/2}$, respectively, indicating a normal state the Fe^{3+} in the two specimens,[3, 13, 14, 28] which strongly confirms no occurrence of carbon thermal reduction of Fe species at high temperature in inert atmosphere. The fitting Zn 2p XPS spectra are presented in **Fig. 2b**. The peaks at BEs of ~1022.1 and ~1045.0 eV can be ascribed to Zn 2p3/2 and Zn 2p1/2, respectively, revealing that the oxidation state of Zn is 2+ in the present ZZFO@C,[13, 14, 28] and another two located at ~1021.4 and ~1044.4 eV should be ascribed to the divalent Zn in the ZnO phase.[13, 35] High-resolution spectrum for the O 1s (**Fig. 2c**) clearly illustrates the three oxygen contributions at ~532.5, ~531.3 and ~530.5 eV, respectively. The peak at ~532.5 eV is attributed to the multiplicity of physi-/chemi-adsorbed water; the one centered at ~531.3 eV is commnonly associated with some defects, under-coordinated lattice oxygen, hydroxyls, and/or chemisorbed oxygen upon the surface of the hybrid ZZFO@C;[36, 37] and the distinct peak located at ~530.5 eV is rationally assigned to typical lattice oxygen in the metal (Zn/Fe)-oxygen framework.[13, 28, 38] In the region of N 1s core level spectrum (**Fig. 2d**), the chemical states of the N atom (3.1 at.%) existing in carbon shell, with BEs of ~400.1 and ~401.8 eV, can be identified as the N-pyrrolic/N-pyridonic and the N-quaternary (N-Q) by using a Gaussian fitting method.[39] And the positive charger on high-content N-Q (1.5 at.%) greatly favors for rapid electron transfer through the core-shell ZZFO@C, beneficial for the enhanced electronic conductivity of the hybrid.[40]

The morphology and structure of the as-obtained ZZFO were examined by FESEM measurement. Apparently, the resultant product is composed of numerous nanospheres with a

diameter range from ~100 to ~450 nm, as seen from representative FESEM images with various magnifications (**Fig. 3a**, **b**), which inherits well the original spherical shape of the ZFC (**Fig. S6a**, ESI†) without any cacination-induced spherical structure alternation. Of particular note, the uneven size distribution observed here would render the as-prepared ZZFO higher tap density, owing to the most compact arrangement.[41] To observe the detailed interior and geometrical structure of ZZFO nanospheres, TEM was applied to take TEM images. Like above FESEM findings, nanospherical structure of a size of ~100 – ~400 nm can be seen from the typical low-magnification TEM image (**Fig. 3c**). Furthermore, the low- and high-magnification TEM images, as displayed in **Fig. 3c-f**, indicate that these nanospheres are actually constructed by lots of nanoparticle (NP) building blocks with polycrystalline characteristics (the inset in **Fig. 3d**), and numerous inter-particle mesopores also can be evidently seen, which is dinstinct evidently from the solid nature of the ZFC (**Fig. S6b**, ESI†). Interestingly, even typical nanospheres with mesoporous yolk-shell structure can be observed in **Fig. 3d**. In particular, a magnifying TEM image (**Fig. 3e**), detected from a sampling region indicated by the blue rectangle in **Fig. 3d**, reveals a visual yolk-shell hollow architecture (**Fig. 3d**, **e**) with a thin shell of ~8 nm in the thickness, as shown in **Fig. 3f**. The formation mechanism of such unique porous and/or yolk-shell nanoarchitecture can be interpreted by the well-known Kirkendall effect based on a non-equilibrium interdiffusion process, as reported previously.[42-44] Over annealing in air, the thermally oxidized decomposition takes place in the internal ZFC, and some gas products like CO_2 and NO_x are generated accordingly, and escape from the inside of solid ZFC nanospheres. In the meanwhile, the diffusion rate of ZFC is different from that of atmospheric oxygen. These factors mentioned above synergistically lead to the formation of mesoporous, and even york-shell hollow architecture. Attractively, such unique hierarchical porous structure is likely to create much more electroactive sites with increased electrochemical surface area, and facilitates the convenient transportation of reactant species during electrochemical Li^+–intercalation/deintercalation processes.

HRTEM examination (**Fig. 3g-i)** clearly displays that the well-developed NP subunits with discernable lattice fringes are attached with each other in various orientations. As seen in **Fig. 3h**, taken from the red rectangle region in **Fig. 3g**, clear lattice fringes in two regions with the spacing are ~0.243 and ~0.247 nm, which can be indexed to (222) crystalline plane of the ZFO and (101) facet of ZnO phase, respectively. Further inspection in **Fig. 3i**, corresponding to the magnified blue square region in **Fig. 3g**, dinstinct spacings of ~0.49 and ~0.24 nm corrsponds to the interplanar distance of (111) crystalline for spinel ZFO and (101) plane of ZnO structure, respectively. These observations above evidently confirm the exitence of intriguing heterojunctions at the nanoscale between the nanosized ZnO and ZFO. In addition, the detected heterojunctions would render an enhanced inner electric field at the interface of ZFO and ZnO phases, which would enhance the electron transfer between these NP subunits over the electrochemical reaction.[45, 46] **Fig. 3j** gives a typical TEM energy dispersive spectrometer (EDS) elemental mapping analysis of two ZZFO nanospheres, distinctly confirming the extremely homogeneous co-existence and uniform elemental distribution of Fe and Zn species from inside to outside in the two adjacent hierarchical mesoporous nanospheres. The corresponding chemical composition of a Fe/Zn ratio of ~3/4 for the mesoporous ZZFO is further confirmed by the energy dispersive X-ray analysis (EDXA) data (**Fig. 3k**). The ratio of ZnO to ZFO is calculated as ~2.1 : 1 in the hybrid ZZFO, with the co-existence of ZFO and ZnO phases in mind. In **Fig. 3l**, the TEM image of ZZFO@C shows that mesoporous ZZFO nanospheres are sucessfully coated with a uniform and continuous thin carbon layer, owing to inherently high affinity of the PDA to ZZFO core,[17] showing a typical core-shell nanostructure. And the thickness of the carbon shell is estimated averagely as ~10 nm, as seen from the high-magnification TEM image (**Fig. 3m**). In addition, one should note that the carbon layer would further effectively prevents the severe agglomeration of the ZZFO core, which results from the intrinsic paramagnetism of the ZFO itself.[17]

The geometrically elemental distribution of as-fabricated core-shell ZZFO@C is further elucidated by the following TEM elemental mapping analysis. The EDS elemental mapping

images (**Fig. 4a**) and EDXA spectrum (**Fig. S8**, ESI†) demonstrate the uniform co-distribution of Fe, Zn, O, C and N components all over the core-shell powder. It is worth much to note that the N-containing carbon also exists in the inner porous channels of the ZZFO core, as visualized in **Fig. 4a**. It is thanks to the inherently mesoporous nature of the ZZFO nanospheres themselves that the dopamine is soaked well into these porous nanospheres, and certain PDA is formed inside accordingly. After annealing treatment in N_2 atmosphere, continuous carbonaceous network would develope well in the interior finally, that is, the N-doped C is not only coated upon the surface of the resultant ZZFO, but exists inside of these porous nanospheres, which can be verified by the corresponding HRTEM image of the hybrid ZZFO@C (**Fig. 4b**). Evidently, besides the visual lattice fringes from ZFO and ZnO, fuscous regions marked by the white ellipsoids should be the amorphouse carbon, and the light regions corresponds to the internal mesopores in the hybrid core-shell ZZFO@C. Furthermore, the bridge-like carbon connections are further evident among these ZZFO@C nanospheres, as observed from **Fig. 4a**. Out of question, such unique structure would form a more contineous conducting network for rapid electron transportation during electrochemical lithium storage.

The porous and textural properties of the as-fabricated ZZFO and ZZFO@C are further investigated by nitrogen adsorption/desorption analyses at 77 K. **Fig. 5** depicts the corresponding sorption isotherms and pore size distribution (PSD) for the two examples. A distinct hysteresis loop with the typical IV sorption behavior can be observed in **Fig. 5a**, suggesting its typical mesoporous feature, according to the International Union of Pure and Applied Chemistry (IUPAC) classification. It is worthy of mentioning that a shift of adsorption step and hysteresis loop towards lower relative pressure observed for the ZZFO@C (~0.45 – 1.0 P/P_0), in contrast to the ZZFO (~0.65 – 1.0 P/P_0), suggests even less porosity and smaller pore size for the ZFFO@C product. As a result, the lower SSA (~43 $m^2\ g^{-1}$) and smaller pore volume (0.11 $cm^3\ g^{-1}$) is obtained for the core-shell hybrid ZZFO@C, owing to the carbon existing in the inner inter-connected pores of the ZZFO sample. And the fitting analysis derives a higher SSA of ~80 m^2

g^{-1} and pore volume of 0.23 m^3 g^{-1} for the ZZFO. Remarkably, the average pore size of the ZZFO@C is estimated as ~6.8 nm by the Barrett–Joyner–Halenda (BJH) method, smaller than that of ~9.1 nm for the ZZFO. The decreased pore size after carbon-coating can be further verified by the PSD data collected in **Fig. 5b**. All in all, the unique mesoporous feature, and interior and/or exterior contineous carbon network will enhance the ZZFO@C/electrolyte contacting sur-/interfaces, shorten the Li^+ and electron difusion length, and efficiently accommodate the strain induced by the volume change during the electrochemical reactions, which would significantly favor for the enhancement of electrochemical performance as high-performance anode materials for advanced LIBs.

3.2 Electrochemical characterization

In view of that the appealing micro-structures and special compositional advantage of the core-shell mesoporous ZZFO@C, as discussed above, are beneficial for LIBs, we next investigate the electrochemical Li-storage properties of the hybrid ZZFO@C nanospheres at room temperature (RT) by using the standard half-battery coin cell (CR2016) *via* CV, galvanostatic charge-discharge and EIS measurements. To better shed light upon the nature and potentials of various structural transformations and typical redox reactions occurring during discharge-charge (*i.e.*, Li insertion/extraction) processes, the electrochemical behaviours of the core-shell ZZFO@C anode were first evaluated by CV technique. **Fig. 6a** describes the representative CV curves of the ZZFO and ZZFO@C nanospheres, respectively, for the first consecutive three cycles at a sweep rate of 0.5 mV s^{-1} in the voltage range of 0.01 – 3.00 V (*vs.* Li/Li^+). Of special note, the initial well-defined cathodic peak position (~0.3 V) for the ZZFO@C shifts negatively somewhat when compared to that of ZZFO (~0.53 V), which should originate from the contribution of N-doped carbon shell. And the two strong reduction peaks both can be generally ascribed to the reduction processes of Fe^{3+} and Zn^{2+} to Fe^0 and Zn^0, respectively, as well as the formation of Li-Zn alloys and Li_2O.[13-15, 17] In the subsequent cycles, same CV profiles are observed distinctly for the two anodes, suggesting their identical reversible Li-storage mechanism over following discharge-charge processes, where the

pronounced cathodic peaks both shift positively and are then located at ~0.86 V, which should be attributed to the reversible reduction reaction of amorphous Fe_2O_3 and ZnO phases. Furthermore, the broad anodic peaks located at ~1.58 V are rationally related to the oxidation of the metallic Zn and Fe into Zn^{2+} and Fe^{3+}, respectively. It is worth noting that the cathodic and/or anodic peaks overlap with each other substantially from the 2nd cycle onward, suggesting the intriguing reversibility of the two for the continuous Li^+-insertion/extraction processes.

Galvanostatic discharge/charge experiments were carried out to evaluate the electrochemical performance of the ZZFO and hybrid ZZFO@C anodes at a current density of 500 mA g^{-1} within a cut-off potential window of 0.01 – 3.00 V (*vs.* Li/Li^+). **Fig. 6b** comparatively demonstrates the representative voltage profiles versus capacity of the 1st, 2nd, and 3rd cycle for the ZZFO and ZZFO@C anodes as indicated. As for the ZZFO anode, the first discharge/charge capacities are ~1178 and ~917 mAh g^{-1}, corresponding to an initial Coulombic efficiency (CE) of 77.8%, which is better than those for other $ZnFe_2O_4$-based anodes (**Table S3**, ESI†), even some hybrids including $NiFe_2O_4/Fe_2O_3$ nanotubes (~71%),[26] Fe_2O_3/Co_3O_4 hollow microcubes (~74.4%),[30] $ZnFe_2O_4/a$-Fe_2O_3 micro-octahedrons (~74.4%),[28] $CoO/CoFe_2O_4$ nano-composites (~70%),[27] *etc*. Moreover, the initial discharge capacity observed here is somewhat higher than its theoretical capacity (~1030 mA g^{-1} = 981 mAh g^{-1} × 45.8 wt.% (ZnO) + 1072 mAh g^{-1} × 54.2 wt.% (ZFO)).[13] which should be partially attibuted to the extra contribution of nanophase co-existing ZnO phase with high content (an intial discharge capacity of ~2300 mAh g^{-1} reported for nanophase ZnO previously[47]). During the subsequent cycle processes, the capacity drops accordingly. At the third cycle, the discharge and charge capacities are down to 960 and 872 mAh g^{-1}, respectively, ~81.5% retention of the initial discharge capacity. In a sharp contrast, the initial discharge/charge capacities of the hybrid ZZFO@C are increased up to ~1392/~1059 mAh g^{-1}, respectively, but along with a low CE of ~76.1% resulting from the repugnant side reactions of the N-doped carbon with the electrolyte, but still higher than those for ZnO/ZFO/C hollow octahedral (~75.6%),[3] ZFO@C/graphene (~67%),[17] ZFO/C hollow spheres (~67%),[48] ZFO/graphene (~64 – ~69%),[49-52] and $NiCo_2O_4$@SnO_2@C

nanostructures (~67%).[53] Also remarkably, similar to those of the ZZFO electrode, the measured dicharge/charge capacity decreases, however, still remains as high as ~1054/~1040 mAh g^{-1} in the case of the ZZFO@C anode.

The excellent rate capability of electrodes is of great significance as one key aspect for application of electric vehicles and smart electrics requiring rapid discharge and/or charge rates. To further explore the rate capabilities, the core-shell ZZFO@C and ZZFO are cycled at progressively increased current rates ranged from 100 to 1500 mA g^{-1} as displayed in **Fig. 6c**. As seen above, the hybrid ZZFO@C exhibits decent lithiation capacity retention with an average discharge capacities of ~1170, ~1072, ~982, and ~878 mAh g^{-1} at current densities of 100, 200, 500 and 1000 mAh g^{-1}, respectively. Even at a rigiously high rate of 1500 mA g^{-1}, a large discharge capacity of ~770 mAh g^{-1} still could be imparted, which indicates that ~66 % of the capacity is even maintained when the current rate is increased from 100 to 1500 mA g^{-1}. More significantly, a high discharge capacity of ~1218 mAh g^{-1} is recovered when the current density is returned to 100 mA g^{-1}. Under the same conditions, the single ZZFO only can deliver ~892, ~732, ~640, ~566 and ~483 mAh g^{-1} at the current density of 100, 200, 500, 1000 and 1500 mA g^{-1}, respectively, that is, the specific capacity of the ZZFO anode just retain as ~54% as the rate is up to 1500 from 100 mA g^{-1}. And only an average capacity of ~772 mAh g^{-1} can be recovered when the current density is further reduced stepwise to 100 mA g^{-1}, as evidence in **Fig. 6c**. It is clear that the rate capacity of the core-shell ZZFO@C is remarkably superior to that of the ZZFO, as seen from the current-rate dependence profiles of discharge capacity (**Fig. S9**, ESI†), which should be rationally related to the smaller charge transfer resistence and better electronic conductivity of the hybrid ZZFO@C than those for ZZFO, benefiting from the unique core-shell mesoporous architecture, as verified by the detailed EIS studies (**Fig. S10**, ESI†) and corresponding fitted data (**Table S4**, ESI†). Also visually, the discharging capacities of the two anodes on each step overlaps welll with the charging counterparts as shown in **Fig. 6c**, suggesting their appealing reversiblities during electrochemical Li^+ insertion-extraction process.

Fig. 6d comparatively describes the cycling performance of the as-prepared ZZFO@C and ZZFO as anode materials at a current density of 500 mAh g^{-1} between 3.00 to 0.01 V versus Li/Li^+ for 60 cycles at RT. After initial fast capacity loss in the first 5 cycles, the core-shell ZZFO@C product maintains stable capacity retention, and even still delivers a discharge capacity as high as ~893 mAh g^{-1} after 60 cycles, *i.e.*, ~64% of capacity retention is obtianed, which is better than that (~61.5%) of the ZZFO under the same testing conditions, that is, ~725 mAh g^{-1} is just remained for the ZZFO over 60 cycles. To further highlight the excellent properties of the ZZFO@C as an anode for high-power LIBs, the longer-term cycling behavior at higher rates are further considered in greater detail for practical application. **Fig. 7** displays the cycling performance and corresponding CE of the core-shell ZZFO@C hybrid anode at a larger current density of 1000 mA g^{-1} over consecutive 500 cycles. As evident, the discharge capacity decreases rapidly during the initial ten discharge-charge cycles and stabilize rapidly at ~800 mA h g^{-1}. More encouragingly, the discharge capacity of the ZZFO@C electrode still remains as ~718 mAh g^{-1} after continuously deep cycling even for 500 times, which is much better than other $ZnFe_2O_4$-based anodes (**Table S3**, ESI†), ordered macroporous $CoFe_2O_4$ (~702 mAh g^{-1} after 30 cycles at 0.2 mA cm^{-2}),[54] quasi-spherical $MgFe_2O_4$ (~290 mAh g^{-1} after 40 cycles at 100 mA g^{-1}),[55] $MnFe_2O_4$ microspheres (~552 mAh g^{-1} after 50 cycles at 740 mA g^{-1}),[56] $NiCo_2O_4$ mesoporous microspheres (~705 mAh g^{-1} after 500 cycles at 800 mA g^{-1}),[12] and even some hybrids including Fe_2O_3/Co_3O_4 (~500 mAh g^{-1} after 50 cycles at 100 mA g^{-1}),[31] Fe_2O_3/SnO_2 nanocombs (~325 mAh g^{-1} after 50 cycles at 400 mA g^{-1}),[57] TiO_2@*a*-Fe_2O_3 core-shell arrays on carbon textiles (~480 mAh g^{-1} after 150 cycles at 120 mA g^{-1}),[58] and so on. Furthermore, the CE has been always maintained nearly 100% during the following continuous lithiation/de-lithiation cycles after the 1st CE of ~77%, indicating its excellent reversibility for electrochemical lithium storage. Attractively, as presented by SEM examination (the inset in **Fig. 7**), the hybrid ZZFO@C basically preserves their core-shell morphology after cycling measurement, just along with the occurrence of some pulverization to some extent in the ZZFO core region, confirming the relative structural stability of the anode again. Combining the

high reversible capacity, high CE and stable cycling performance at large current rate, we rationally believe that the core-shell mesoporous ZZFO@C is a promising superior candidate as an anode material for next-generation LIBs.

The outstanding lithium-storage properties of the core-shell ZZFO@C nanospheres should originate from the synergistic effect of their unique constituent and structural advantages, as schematically presented in **Fig. 8**, including following several aspects: (I) the inter-connected mesoporous, and even yolk-shell hollow structure in the core-shell hybrid would ensure the presence of additional free volume/void to alleviate the structural strain associated with repeated Li^+ insertion/extraction processes, and shorten the Li^+ diffusion length, as well as a high availability of the electroactive sur-/interface contact between electrode and electrolyte. (II) A number of heterojunctions between nanophase ZFO and ZnO render a high electrical conductivity of the whole anode itself.[45, 46] Additionally, high-content ZnO NPs, as well-dispersed buffer domains, can spatially separate,[13, 27, 59] and further prevent self-aggregation of the co-existing nanosized ZFO with high electroactivity at the nanoscale. (III) The presence of the robust and flexible N-doped carbon nanocoating shell enhances the structural stability and electrode conductivity, prevents partial aggregation, and stabilizes the SEI film.[22, 60] Furthermore, the interconnected carbon matrix throughout the internal ZZFO@C helps to relieve the volume effect during the lithium insertion/extraction processes, and maintains electrical connectivity integrity.

4. Conclusions

In conclusion, herein, we rationally designed and successfully fabricated N-doped carbon coating ZZFO nanospheres, *i.e.*, multi-featured core-shell ZZFO@C nano-architectures for advanced LIBs as an intriguing anode. Remarkably, such unique hybrid structure incorporates several design rationales for well-defined anode materials, including mesoprous and/or yolk-shell hollow ZZFO core, uniform N-doped carbon shell nanopainting, mixed ZnO-ZFO heterojunctions at the nanocale, and interconnected carbon matrix throughout the internal ZZFO, which reduced the

diffusion length for Li^+, improved the kinetic process and enhanced the structural integrity with sufficient void space for tolerating the volume variation during the Li^+ insertion/extraction. In favor of the appealing synergetic effects of intrinsic component and structure advantages, the as-obtained core-shell ZZFO@C mesoporous nanospheres exhibited outstanding electrochemical Li-storage behaviors including high CE, exceptional cycling performance and enhanced high-rate capacibility for advanced LIBs. Of great significance, we also envision that the smart electrode design concept can be easily generalized to other hierarchical core-shell hybrids for next-generation LIBs.

Acknowledements

The authors acknowledge the financial support from National Natural Science Foundation of China (no. 51202004, 51572005, 51502003). Anhui Province Funds for Distinguished Young Scientists (no. 1508085J09), the Natural Science Foundation of Anhui Province (no. 1508085ME106, KJ2013A051), the Foundation for Young Talents in College of Anhui Province, and the Opening Project of CAS Key Laboratory of Materials for Energy Conversion (no. 2014001).

Supporting information

† Electronic Supplementary Information (ESI) available: XRD, TG, Raman, EDXA, XPS, FESEM and TEM images, EIS data of the controlled experiments. See DOI: 10.1039/b000000x/

Notes and references

[1] M. Armand and J. M. Tarascon, *Nature*, 2008, **451**, 652.

[2] C. Z. Yuan, H. B. Wu, Y. Xie and X. W. Lou, *Angew. Chem. Int. Ed.*, 2014, **53**, 1488.

[3] F. Zou, X. L. Hu, Z. Li, L. Qie, C. C. Hu, R. Zeng, Y. Jiang and Y. H. Huang, *Adv. Mater.*, 2014, **26**, 6622.

[4] M. R. Palacín, *Chem. Soc. Rev*., 2009, **38**, 2565.

[5] P. Poizot, S. Laruelle, S. Grugeon, L. Dupon and J. M. Tarascon, *Nature*, 2000, **407**, 496.

[6] Z. L. Zhang, Q. Q. Tan, Y. F. Chen, J. Yang and F. B. Su, *J. Mater. Chem. A*, 2014, **2**, 5041.

[7] G. Q. Zhang, L. Yu, H. B. Wu, H. E. Hoster and X. W. Lou, *Adv. Mater.*, 2012, **24**, 4609.

[8] C. Z. Yuan, L. H. Zhang, L. R. Hou, L. Zhou, G. Pang and L. Lian, *Eur.-Chem. J.*, 2015, **21**, 1262.

[9] C. Z. Yuan, L. H. Zhang, H. Cao, S. Q. Zhu, J. D. Lin and L. R. Hou, *Nanotechnology*, 2015, **26**, 145401.

[10] L. F. Shen, L. Yu, X. Y. Yu, X. G. Zhang and X. W. Lou, *Angew. Chem. Int. Ed.*, 2015, **54**, 1868

[11] B. Liu, J. Zhang, X. F. Wang, G. Chen, D. Chen, C. W. Zho and G. Z. Shen, *Nano Lett.*, 2012, **12**, 3005.

[12] J. F. Li, S. L. Xiong, Y. R. Liu, Z. C. Ju and Y. T. Qian, *ACS Appl. Mater. Interfaces*, 2013, **5**, 981.

[13] L. R. Hou, L. Lian, L. H. Zhang, G. Pang, C. Z. Yuan and X. G. Zhang, *Adv. Funct. Mater.*, 2015, **25**, 238.

[14] L. Lian, L. R. Hou, L. Zhou, L. S. Wang and C. Z. Yuan, *RSC Adv.*, 2014, **4**, 49212.

[15] J. M. Won, S. H. Choi, Y. J. Hong, Y. N. Ko and Y. C. Kang, *Sci. Rep.*, 2014, **4**, 5857.

[16] Z. L. Zhang, Y. J. Li, J. Li, Q. Q. Tan, Z. Y. Zhong and F. B. Su, *ACS App. Mater. Interfaces*, 2015, **7**, 6300.

[17] L. Lin and Q. M. Pan, *J. Mater. Chem. A*, 2015, **3**, 1724.

[18] R. M. Thankachan, M. M. Rahman, I. Sultana, A. M. Glushenkov, S. Thomas, N. Kalarikkal and Y. Chen, *J. Power Sources*, 2015, **282**, 462.

[19] Z. Xing, Z. C. Ju, J. Yang, H. Y. Xu and Y. T. Qian, *Nano Res.*, 2012, **2**, 477.

[20] L. R. Hou, H. Hua, L. Lian, H. Cao, S. Q. Zhu and C. Z. Yuan, *Eur.-Chem. J.*, 2015, DOI:10.1002/chem.201501876.

[21] A. Varzi, D. Bresser, J. Von Zamory, F. Muller and S. Passerini, *Adv. Energy Mater.*, 2014, **4**, DOI: 10.1002/aenm.201400054.

[22] Z. Y. Wang, Z. C. Wang, W. T. Liu, W. Xiao and X. W. Lou, *Energy Environ. Sci.*, 2013, **6**, 87.

[23] A. Mahbuba, R. C. Venkateswara, S. O. Salley and K. Y. S. Ng, *Electrochim. Acta*, 2015, **161**, 269.

[24] Y. Hou, J. Y. Li, Z. H. Wen, S. M. Cui, C. Yuan and J. H. Chen, *Nano Energy*, 2015, **12**, 1.

[25] M. A. Woo, T. W. Kim, I. Y. Kim and S. J. Hwang, *Solid State Ionics*, 2011, **182**, 91.

[26] G. Huang, F. F. Zhang, L. L. Zhang, X. C. Du, J. W. Wang and L. M. Wang, *J. Mater. Chem. A*, 2014, **2**, 8048.

[27] M. X. Li, Y. X. Yin, C. J. Li, F. Z. Zhang, L. J. Wan, S. L. Xu and D. G. Evans, *Chem. Commun.*, 2012, **48**, 410.

[28] D. Zhao, Y. Xiao, X. Wang, Q. Gao and M. H. Cao, *Nano Energy*, 2014, **7**, 124.

[29] X. Gu, L. Chen, Z. C. Ju, H. Y. Xu, J. Yang and Y. T. Qian, *Adv. Funct. Mater.*, 2013, **23**, 4049.

[30] Z. Q. Li, B. Li, L. W. Yin and Y. X. Qi, *ACS Appl. Mater. Interfaces*, 2014, **6**, 8098.

[31] Z. Y. Wang, L. Zhou and X. W. Lou, *Adv. Mater.*, 2012, **24**, 1903.

[32] X. W. Lou, L. A. Archer and Z. C. Yang, *Adv. Mater.*, 2008, **20**, 3987.

[33] H. Lee, S. M. Dellatore, W. M. Miller and P. B. Messersmith, *Science*, 2007, **318**, 426.

[34] C. Lei, F. Han, D. Li, W. C. Li, Q. Sun, X. Q. Zhang and A. H. Lu, *Nanoscale*, 2013, **5**, 1168.

[35] X. H. Liu, J. Zhang, L. W. Wang, T. L. Yang, X. Z. Guo, S. H. Wu and S. R. Wang, *J. Mater. Chem.*, 2011, **21**, 349.

[36] C. Z. Yuan, J. Y. Li, L. R. Hou, X. G. Zhang, L. F. Shen and X. W. Lou, *Adv. Funct. Mater.*, 2012, **22**, 4592.

[37] C. Z. Yuan, J. Y. Li, L. R. Hou, J. D. Lin, X. G. Zhang and S. L. Xiong, *J. Mater. Chem. A*, 2013, **1**, 11145.

[38] Y. Sharma, N. Sharma, G. V. Subba Rao and B. V. R. Chowdari, *Electrochim. Acta*, 2008, **53**, 2380.

[39] L. Zhou, S. Q. Zhu, H. Cao, L. R. Hou and C. Z. Yuan, *Green Chem.*, 2015, **17**, 2373.

[40] D. Hulicova-Jurcakova, M. Seredych, G. Q. Lu and T. J. Bandosz, *Adv. Funct. Mater.*, 2009, **19**, 438.

[41] C. Z. Yuan, J. Y. Li, L. R. Hou, L. H. Zhang and X. G. Zhang, *Part. Part. Syst. Charactert.*, 2014, **31**, 657.

[42] N. Yan, L. Hu, Y. Li, Y. Wang, H. Zhong, X. Y. Hu, X.K. Kong and Q. W. Chen, *J. Phys. Chem. C*, 2012, **116**, 7227.

[43] Y. D. Yin, R. M. Rioux, C. K. Erdonmez, S. Hughes, G. A. Somorjai and A. P. Alivisatos, *Science*, 2004, **304**, 711.

[44] H. J. Fan, M. Knez, R. Scholz, D. Hesse, K. Nielsch, M. Zacharias and U. Gosele, *Nano Lett.*, 2007, **7**, 993.

[45] L. Qiao, X. H. Wang, L. Qiao, X. L. Sun, X. W. Li, Y. X. Zheng and D. Y. He, *Nanoscale*, 2013, **5**, 3037.

[46] L. J. Lauhon, M. S. Gudiksen, D. Wang and C. M. Lieber, *Nature*, 2002, **420**, 57.

[47] S. J. Yang, S. Nam, T. Kim, J. H. Im. H. Jung, J. H. Kang, S. G. Wi and B. Park, *J. Am. Chem. Soc.*, 2013, **135**, 7394.

[48] Y. F. Deng, Q. M. Zhang, S. D. Tang, L. T. Zhang, S. N. Deng, Z. C. Shi and G. H. Chen, *Chem. Commun.*, 2011, **47**, 6828.

[49] W. T. Song, J. Xie, S. Y. Liu, G. S. Cao, T. J. Zhu and X. B. Zhao, *New J. Chem.*, 2012, **36**, 2236.

[50] H. Xia, Y. Y. Qian, Y. S. Fu and X. Wang, *Solid State Sci.*, 2013, **17**, 67.

[51] J. Xie, W. T. Song, G. S. Cao, T. J. Zhu, X. B. Zhao and S. C. Zhang, *RSC Adv.*, 2014, **4**, 7703.

[52] J. J. Shi, X. Y. Zhou, Y. Liu, Q. M. Su, J. Zhang and G. H. Du, *Mater. Res. Bull.*, 2015, **65**, 204.

[53] G. X. Gao, H. B. Wu, S. J. Ding and X. W. Lou, *Small*, 2015, **11**, 432.

[54] Z. H. Li, T. P. Zhao, X. Y. Zhan, D. S. Gao, Q. Z. Xiao and G. T. Lei, *Electrochim. Acta*, 2010, **55**, 4594.

[55] H. W. Liu and H. F. Liu, *J. Electron. Mater.*, **2014**, DOI: 10.1007/s11664-014-3117-2.

[56] Z. L. Zhang, Y. H. Wang, Q. Q. Tan, Z. Y. Zhong and F. B. Su, *J. Colloid Interface Sci.*, 2013, **398**, 185.

[57] Y. L. Wang, J. J. Xu, H. Wu, M. Xu, Z. Peng and G. F. Zheng, *J. Mater. Chem.*, 2012, **22**, 21923.

[58] Y. S. Luo, J. S. Luo, J. Jiang, W. W. Zhou, H. P. Yang, X. Y. Qi, H. Zhang, H. J. Fan, D. Y. W. Yu, C. M. Li and T. Yu, *Energy Environ. Sci.*, 2012, **5**, 6559.

[59] M. A. Woo, T. W. Kim, I. Y. Kim and S. J. Hwang, *Solid State Ionics*, 2011, **182**, 91.

[60] H. Q. Li and H. S. Zhou, *Chem. Commun.*, 2012, **48**, 1201.

Figures and Captions

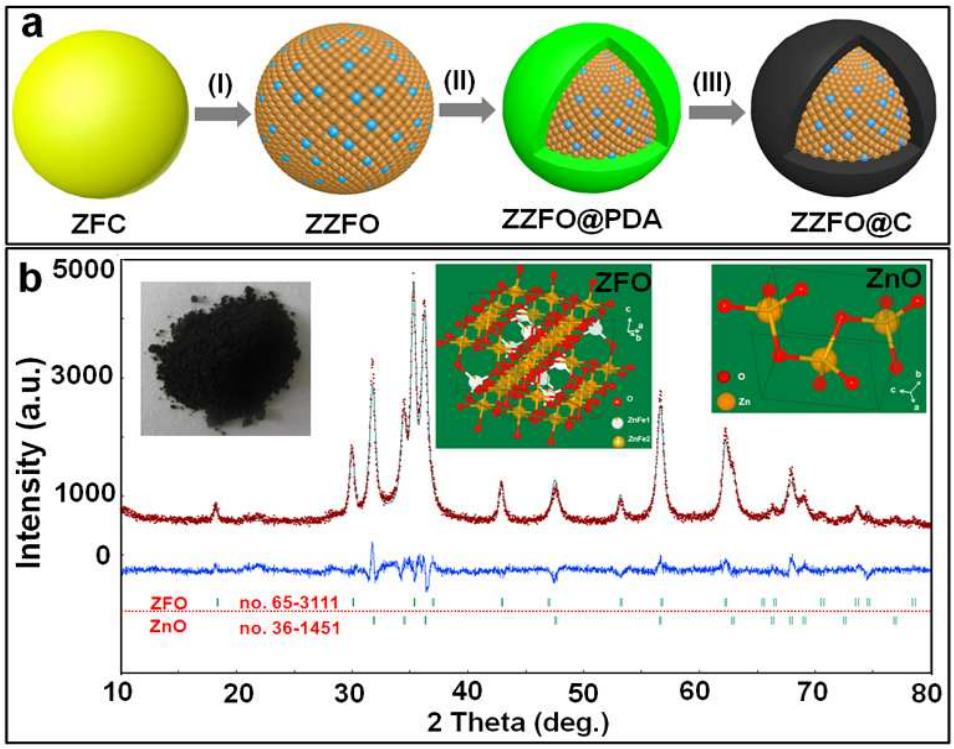

Fig. 1. Schematic illustration for synthetic procedure of core-shell ZZFO@C hybrid (a), and corresponding Rietveld refine pattern (b). Experimental data, calculated profile and their difference are highlighted as wine crosses, cyan and blue solid lines, respectively. Short green vertical bars for the standard JCPDS data of ZFO (no. 65-3111) and ZnO (no. 36-1451). The insets in panel (b) for the optical image of the resultant ZZFO@C hybrid, and typical crystallographic structures for the ZFO and ZnO as indicated

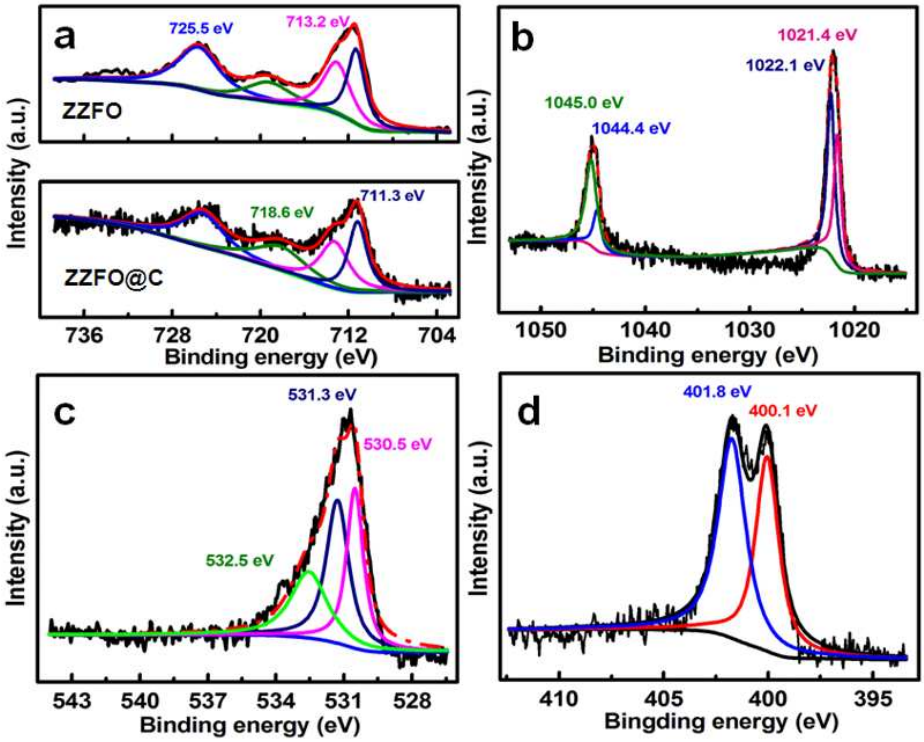

Fig. 2. XPS spectra and corresponding fitting curves of the ZZFO@C (a-d) and ZZFO (a) samples as indicated. (a) Fe 2p; (b) Zn 2p; (c) O 1s and (d) N1s

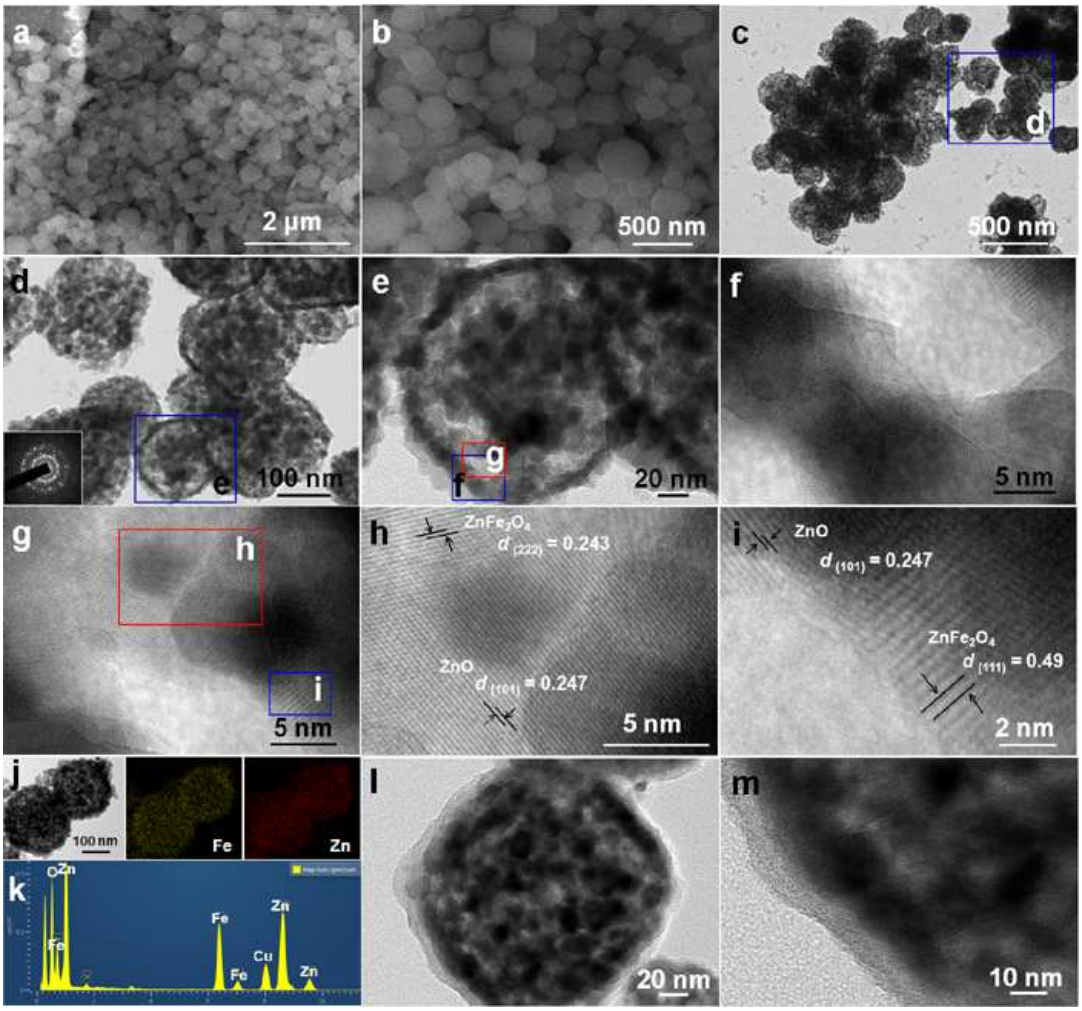

Fig. 3. FESEM (a, b), TEM (c−e), HRTEM (f−i), selected TEM area for the element mapping and elemental (Fe, Zn) mapping (j) images, and EDXA spectrum (k) of the as-fabricated ZZFO nanospheres. TEM images (l, m) of the core-shell ZZFO@C nanospheres. The inset in panel (d) for SAED pattern for the resulting ZZFO

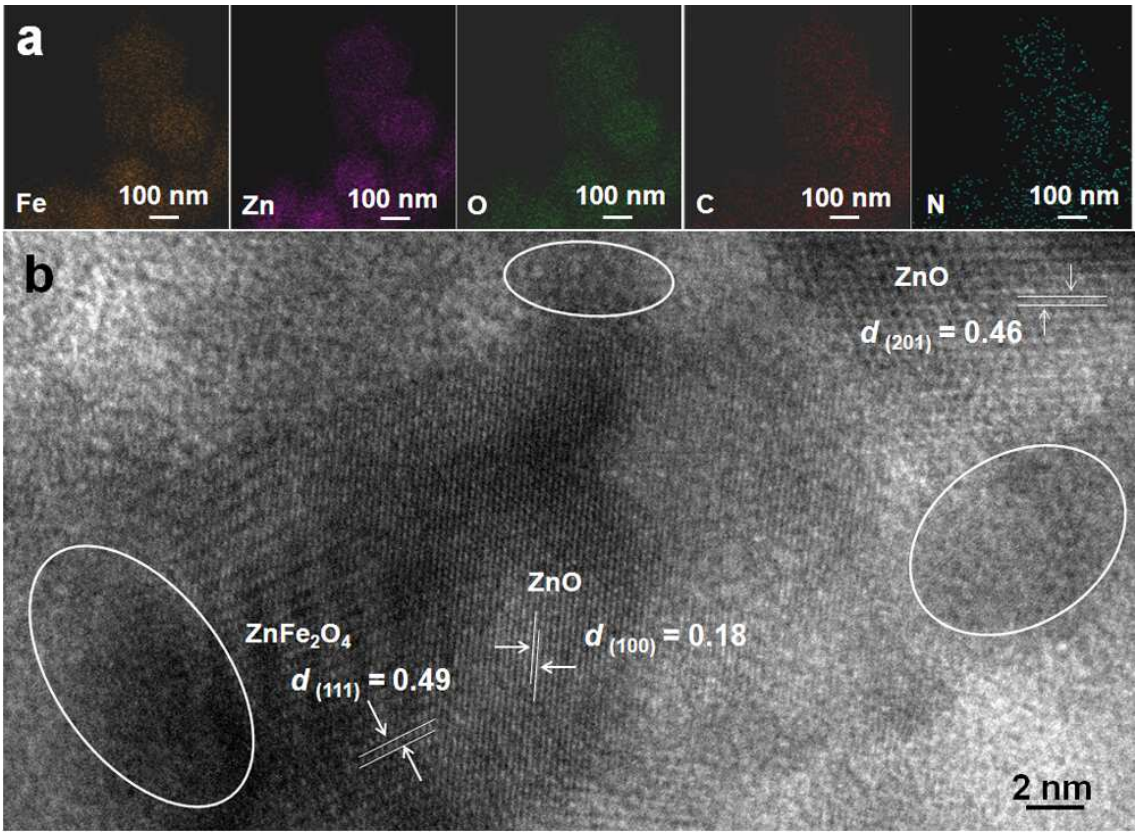

Fig. 4. Selected TEM EDS elemental (Fe, Zn, O, C and N) mapping images (a) and HRTEM image (b) of the core-shell ZZFO@C product

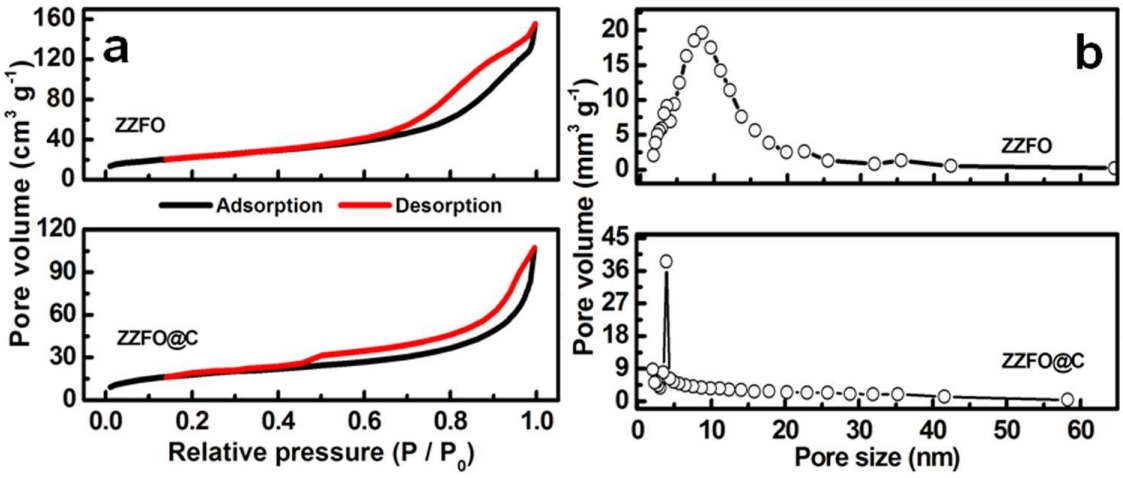

Fig. 5. N_2 adsorption-desorption isotherms (a) and PSD data (b) of the ZZFO@C and ZZFO as indicated

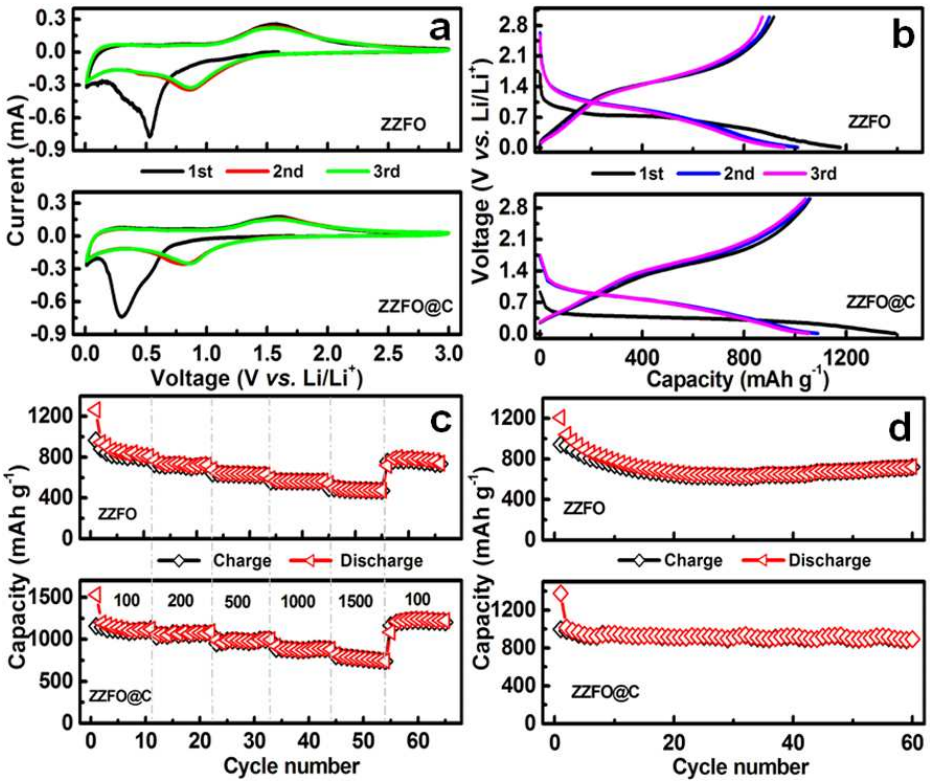

Fig. 6. Electrochemical performance of the ZZFO and ZZFO@C samples: The first three consecutive CV curves (a, 0.5 mV s^{-1}) and discharge-charge profiles (b, 500 mA g^{-1}), rate capability testing at various rates from 100 to 1500 mA g^{-1} (c), and cycling performance (d, 500 mA g^{-1}) of the ZZFO and ZZFO@C anodes as indicated

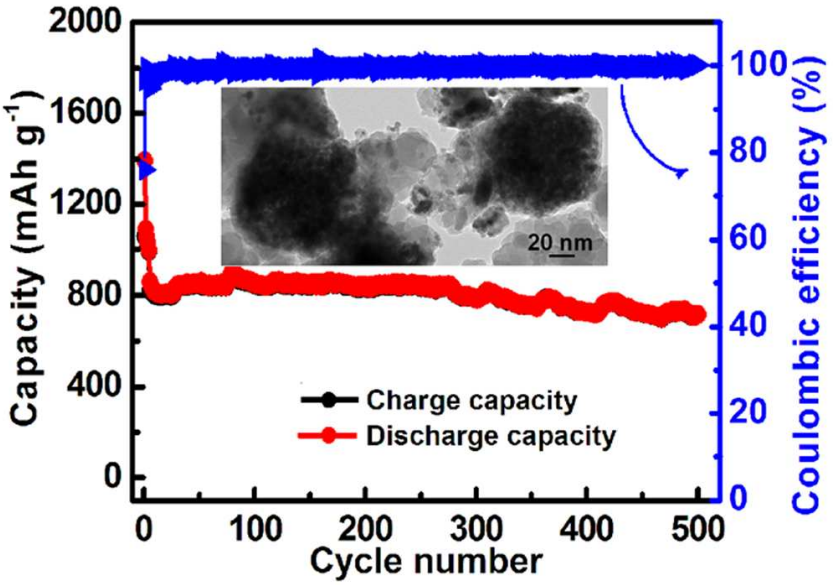

Fig. 7. Discharge/charge capacities and corresponding CE versus cycle number of the core-shell ZZFO@C mesoporous nanospheres at a large current density of 1000 mA g^{-1}. The inset for the TEM image of the core-shell ZZFO@C nanospheres after cycling test

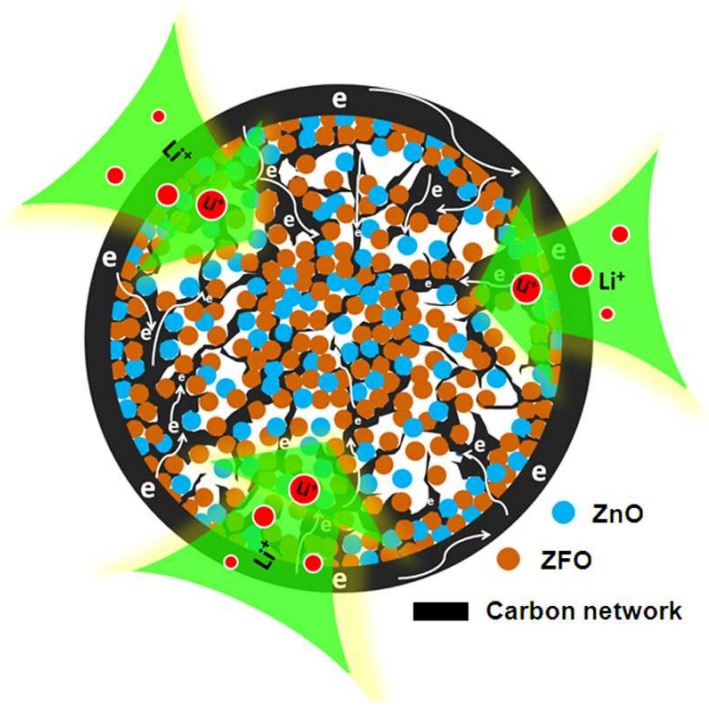

Fig. 8. Schematic illustration and operating principles of the unique core-shell mesoporous ZZFO@C anode for LIBs

The Table of Contents entry

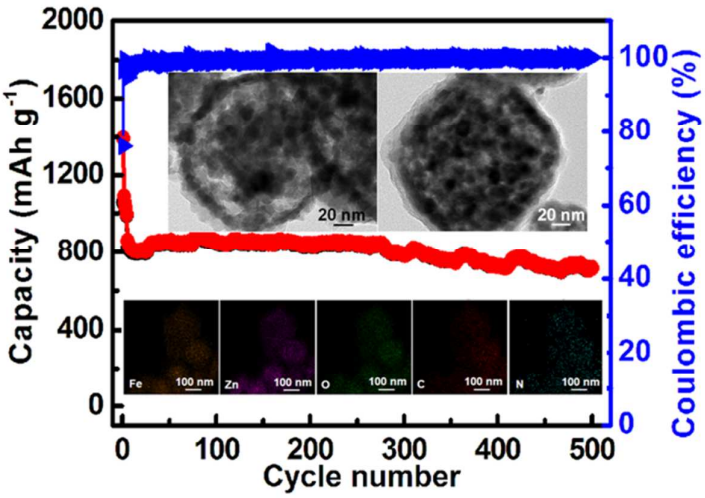

Core-shell ZnO/$ZnFe_2O_4$@C mesoporous nanospheres were rationally fabricated, and exhibited exceptional electrochemical Li-storage performance with high reversible capacity, excellent stability and appealing rate property for next-generation Li-ion batteries